



Article

Vis and NIR Diffuse Reflectance Study in Disordered Bismuth Manganate—Lead Titanate Ceramics

Andrzej Molak * , Anna Z. Szeremeta and Janusz Koperski

August Chełkowski Institute of Physics, University of Silesia in Katowice, ul. 75 Pułku Piechoty 1, 41-500 Chorzów, Poland; anna.szeremeta@us.edu.pl (A.Z.S.); janusz.koperski@us.edu.pl (J.K.)

* Correspondence: andrzej.molak@us.edu.pl; Tel.: +48-32-3497638

Abstract: This work shows a correlation between light reflectance, absorption, and morphologies of series of bismuth manganate–lead titanate, $(1 - x)$ BM– x PT, ($x = 0.00, 0.02, 0.04, 0.08, 0.12, 0.16, 0.24, 1.00$) ceramics composite. Low reflectance in the Vis–NIR range corresponds to ‘black mirror’ features. The modified Kubelka–Munk function applied to measured visible–near infrared (Vis–NIR) diffuse reflectance enabled the estimation of the energy gaps magnitude of the order of 1.0–1.2 eV for BM–PT. Histograms of grains, obtained using a scanning electron microscope, enabled finding the correlation between grains size, reflectance magnitude, and PT content. The magnitude of energy gaps was attributed to electronic structure bands modified by crystal lattice disorder and oxygen vacancies.

Keywords: bismuth manganate; ceramics composite; lead titanate; energy gap; surface morphology; Vis–NIR reflectance



Citation: Molak, A.; Szeremeta, A.Z.; Koperski, J. Vis and NIR Diffuse Reflectance Study in Disordered Bismuth Manganate—Lead Titanate Ceramics. *Electron. Mater.* **2022**, *3*, 101–114. <https://doi.org/10.3390/electronicmat3010010>

Academic Editor: Jai Singh

Received: 28 October 2021

Accepted: 17 February 2022

Published: 25 February 2022

Publisher’s Note: MDPI stays neutral with regard to jurisdictional claims in published maps and institutional affiliations.



Copyright: © 2022 by the authors. Licensee MDPI, Basel, Switzerland. This article is an open access article distributed under the terms and conditions of the Creative Commons Attribution (CC BY) license (<https://creativecommons.org/licenses/by/4.0/>).

1. Introduction

Perovskite ABO_3 oxide materials attract attention for solar cells research and development and photovoltaic studies. The energy gap, E_{gap} , which separates the energies of the valence band, VB, maximum, and conduction band minimum, determines the material possibilities for such applications [1]. Electronic structure tuning is necessary for many materials to obtain suitable optical E_{gap} demanded for optical applications. The power conversion high efficiency also depends on the long lifetimes of excited charge carriers, which allows travel across long distances prior to recombination. Moreover, in accord to the Shockley–Queisser limit, the highest efficiency is reached at a band gap energy of 1.34 eV [2,3].

The ABO_3 VB is formed by oxygen O 2p states hybridized with states of metal 3d, 4d, and 5d placed in the B position. The 4d and 5d metal ions placed in B sublattice usually form a wide gap in the electronic structure. For instance, several perovskite titanates and niobates show insulator E_{gap} of the order of 3 eV and ultraviolet, UV, light range only is available for energy harvesting, due to limited light absorption in Vis range. It is worth noting that the light energies higher than the Vis–UV limit are insufficient for photovoltaic applications.

The wide gap ferroelectric perovskites provide low electrical conductivity and negligible dielectric losses. Moreover, it should be noticed that ferroelectric ordering enhances absorption efficiency due to empty d^0 shells crucial for the formation of the ferroelectric state, which exerts a weak force on the moving charge carriers. Simultaneously, when the electron–hole pairs are formed after photon absorption, the electrons and holes can be separated and pushed towards opposite directions by the electric fields of the internal polarization [4–6].

Contrary, the narrow band perovskites can be obtained from the oxides of the metal ions from the 3d group, e.g., Fe, Mn, Cr, and Co. They offer better ability, including absorption in Vis and NIR, range. However, narrow optical E_{gap} results in low activation

energy in electric conductivity, which induces marked electrical cross-current flow and losses [7–19].

There are several routes to modify the optical E_{gap} of oxide ABO_3 materials. Demanded properties can be obtained when materials exhibiting different E_{gap} magnitude are combined. Consequently, composites formed from oxide materials, which show large and narrow E_{gap} , respectively, allow modifying the optical properties because the narrower gap may enhance light absorbance efficiency in the Vis-NIR range. The substitution of the metal ions can lead either to solid solutions or the formation of precipitates. Minor phases may appear when the solubility limit is overstepped, and/or a transformation of the phases occurs [15,20]. The electronic structure can also be modified by an additional treatment that can change the concentration of the oxygen vacancies, V_{O} defects [21–23]. The V_{O} forms shallow and deep energy levels within the E_{gap} , increasing both absorbance at lower energies and electrical losses [24]. For instance, the active role of the $\text{Mn}^{2+}/\text{Mn}^{3+}$ in capturing photons in the NIR spectrum in the case of, e.g., multilayer $\text{Bi}(\text{Fe}_{1-x}\text{Mn}_x)\text{O}_3$ photonic crystals and Mn-doped TiO_2 was analyzed [20,25–27].

From such points of view, narrow gap manganates and wide gap ferroelectric perovskites attract attention for photovoltaic applications [6,17,20,28]. In our study, we have chosen BM and PT to obtain ceramics composite. We presumed that ferroelectric PT addition to semiconductor BM would affect the electronic structure and influence light reflectance and absorption efficiency.

The PT shows a tetragonal $P4mm$ phase at room temperature. Ferroelectric-paraelectric phase transition, which occurs in 763 K, points to the high stability of this compound ferroelectric phase. PT crystal is the ferroelectric insulator showing measured optical $E_{\text{gap}} = 3.4$ eV [29–31]. The tuning of the energy gap was achieved by defects and doping control. The Mn-doped PT crystals exhibited optical E_{gap} lowered to 2.0–2.7 eV, attributed to the occurrence of V_{O} and dipole $\text{Mn}^{k+}-V_{\text{O}}$ defects [32]. The defected crystal, that is, $\text{N}-V_{\text{O}}$ co-doped PT, showed the experimental $E_{\text{gap}} = 2.93$ eV [29]. The PT powder, which was used for the sintering of the BM-PT ceramic, was obtained from hydrothermal growth [33].

BM structure depends on growth conditions [34–36]. We sintered BM ceramics in standard high-temperature ambient air conditions, and a thermodynamically stable two-phase self-composite compound was obtained. Occurrence of two phases in equilibrium: 38% of the cubic $I23$ with the $\text{Bi}_{12}\text{MnO}_{20}$ composition and 62% of the orthorhombic $Pbam$ with the BiMn_2O_5 composition were determined [37]. The self-composite BM was an electrically non-polar compound, which exhibited antiferromagnetic order in a low-temperature range with $T_{\text{Néel}} \approx 39$ K [38]. In accordance with the literature, the BiMn_2O_5 phase exhibited $E_{\text{gap}} = 1.24$ eV for thin films [39], and $E_{\text{gap}} = 1.61$ eV, for nano-grain material [40]. The $E_{\text{gap}} = 0.78$ eV [41] and $E_{\text{gap}} = 1.23$ eV [42] was calculated dependably on the modeling method. The sillenite $\text{Bi}_{12}\text{MnO}_{20}$ exhibits intrinsic $E_{\text{gap}} = 1.86$ eV, intermediate band related to the gap of ~ 1.07 eV, and VB placed 1.4 eV below the Fermi level [43]. It should be noted that the $E_{\text{gap}} = 1.1$ eV was estimated for the thin film perovskite BiMnO_3 variance [27,44]. Moreover, differences in energy states related to a material's particular phases would be determined since their contribution can manifest as a superposition in the spectral response [44]. Therefore, diffuse reflectance of the $(1-x)$ BM- x PT composite ceramics should be determined in the Vis and NIR ranges of the photon spectrum.

A series of $(1-x)$ BM- x PT, ($x = 0.00, 0.02, 0.04, 0.08, 0.12, 0.16, 0.24, 1.00$) ceramics was sintered previously and their phases were determined using XRD, SEM, and dielectric impedance tests [45–47]. In this work, we studied diffuse reflectance in the Vis-NIR range to determine the PT content influence on the BM-PT composite absorption coefficient magnitude. It should be noted that the reflectance magnitude also depends on the properties of the surface exposed to the incident light. Hence, we determined ceramics' morphology using scanning electron microscopy. This manuscript discusses the correspondence between light reflectance, estimated absorption coefficient energy gap, ceramics', and morphology.

2. Materials and Methods

2.1. Preparation of Composite Ceramics

A series of $(1 - x)$ BM- x PT ($x = 0.00, 0.02, 0.04, 0.08, 0.12, 0.16, 0.24, 1.00$) ceramics was produced via standard high temperature sintering. A two-stage procedure was performed. BM ceramics [48] and PT powder [33] were prepared separately at the first step. BM ceramics were produced using high-temperature sintering in the air ($T_S = 1170$ K for 2 h), according to the nominal BiMnO_3 formula [49]. They were graphite-like in color. The stoichiometric PT powder, which showed grains of sizes on submicron level (<500 nm), was obtained from the hydrothermal synthesis. It exhibited tetragonal $P4mm$ symmetry [33]. The reference PT pellets were produced, and they were light yellow in color. Then the BM and PT powders were mixed in stoichiometric ratio, milled for 1 h, and pressed to pellets at 20 MPa. The ceramics were sintered at $T_S = 1170$ K in ambient air for 1 h [46,50]. The sintered BM-PT ceramics were hard, porous, and graphite-like in color. The structure of phases was determined using X-ray diffraction patterns in previous works [46,48,50].

2.2. Vis-NIR Reflectance

A USB-650 VIS-NIR Optic Spectrometer (OceanInsight, Inc., Orlando, FL, USA) equipped with a krypton light source lamp and OceanView 2.0 software was used. The Vis-NIR diffuse reflectance, R , spectra of the samples (~ 1 mm thick) were recorded in the wavelengths, λ , 400–1000 nm range at room temperature. The absorption coefficient was calculated from the reflectance spectra. The optical absorbance spectra were evaluated and presented using a Tauc plot of the modified Kubelka-Munk function to determine the optical band gap.

2.3. Surface Morphology

A scanning microscope JSM-5410 equipped with an energy dispersion X-ray spectrometer (EDS with Si (Li) X-ray detector) was used to characterize the morphology and elemental content. The measuring chamber vacuum was 10^{-4} – 10^{-5} Pa.

3. Results

3.1. SEM Morphology

The grains' morphology of series x BM- $(1 - x)$ PT ceramics was studied using SEM. The ceramics showed a variety of grain shapes: cubes, hexagon base polyhedrons, and tiny irregular forms. The voids and porosity were observed in ceramics surfaces.

Figure 1 shows secondary electron images obtained for the reference BM and PT ceramics. The BM map shows polyhedral-shaped hexagonal base grains with different sizes, varying predominantly in 0.2–2.0 μm in transverse dimension and 0.3–4.0 μm in longitudinal dimension, which is clearly visible in obtained polyhedrons grain size distribution (Figure 1a). There is a low number of grains with longitudinal size above 6.0 μm . The PT ceramics show homogenous morphology (Figure 1b). However, the grains' size is markedly smaller, lower than 1.0 μm .

The 0.98 BM-0.02 PT ceramics (Figure 2a) shows variation in grain size similar to the pure BM ceramics. The obtained distribution shows that the grain transverse dimension is mostly between 0.5–2.5 μm . The longitudinal dimension is mostly between 0.2 and 3.5 μm . There is a low number of larger grains with sizes reaching 6.5 μm . On the contrary, the 0.96 BM-0.04 PT ceramics exhibits a higher number of small grains (Figure 2b). Moreover, obtained grains size distributions show an increased number of larger size grains compared to the previous composition. Namely, grain' transverse dimension is mostly between 1.0–5.0 μm , and the longitudinal dimension is mostly between 0.5 and 4.0 μm . There are several large grains with longitudinal sizes above 10.0 μm .

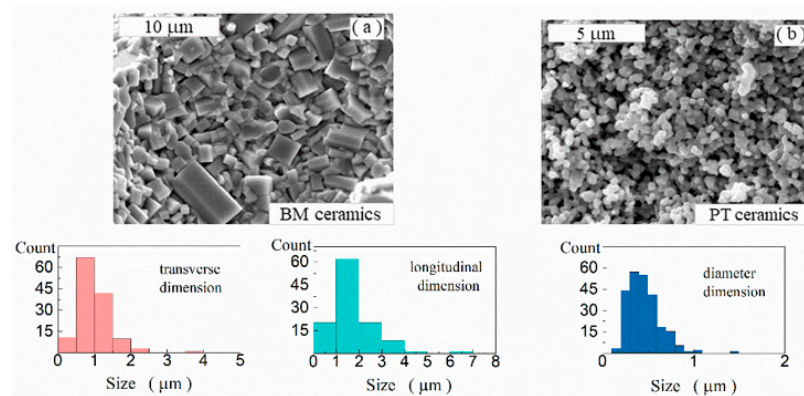


Figure 1. Secondary electron images obtained for BM ceramics (a) and PT ceramics (b). Histograms show grains' transverse, longitudinal, and diameter size distribution.

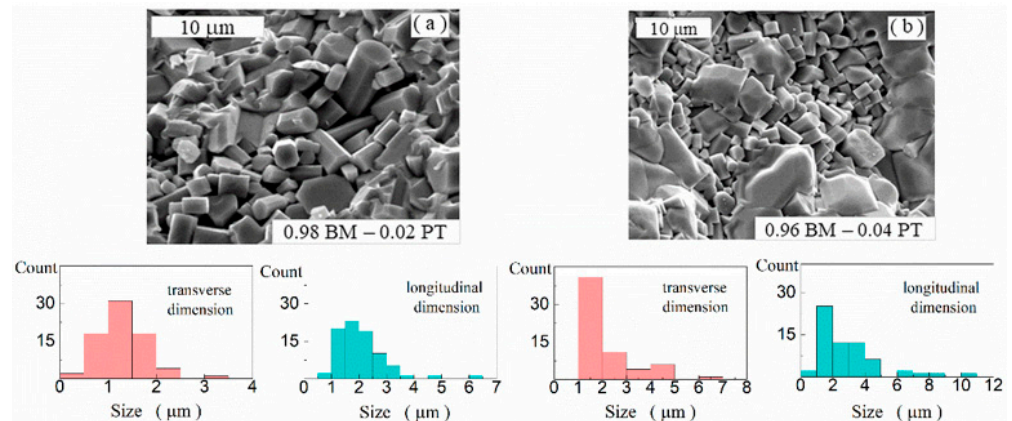


Figure 2. Secondary electron images obtained for 0.98 BM–0.02 PT ceramics (a) and 0.96 BM–0.04 PT ceramics (b). Histograms show grains' transverse and longitudinal size distribution.

Figure 3a,b show similar morphology of 0.92 BM–0.08 PT and 0.88 BM–0.12 PT ceramics, respectively. The obtained histograms show that the amount of the grain' of transverse varies between 0.3–3.0 μm for both ceramics. The longitudinal dimension distribution is slightly different when compared for these two ceramics and varies between 1.0–5.5 μm for 0.92 BM–0.08 PT and 1.0–4.5 μm for the 12% of PT. There are no large grains with longitudinal size above 6.0 μm, which occur for the ceramics with a low amount of dopant PT (compare Figures 2 and 3).

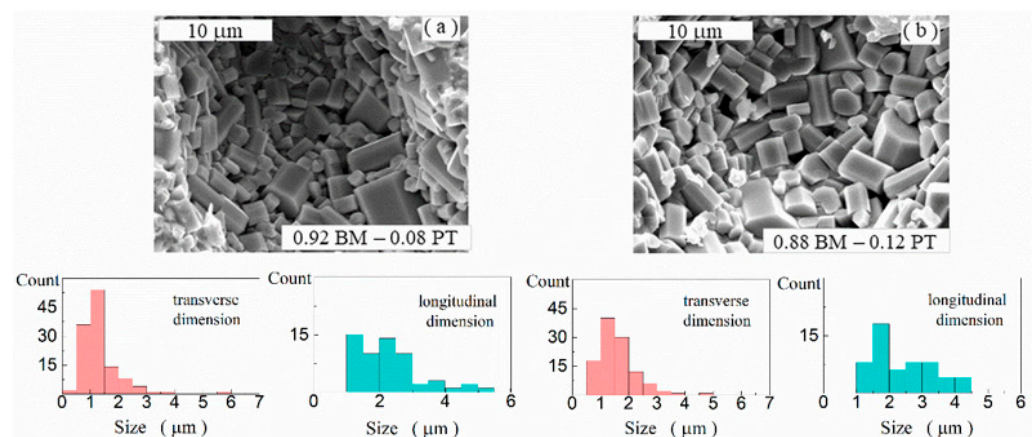


Figure 3. Secondary electron images obtained for 0.92 BM–0.08 PT ceramics (a) and 0.88 BM–0.12 PT ceramics (b). Histograms show grains' transverse and longitudinal size distribution.

The obtained results for the high contents of PT are shown in Figure 4a,b. We can see that the 0.84 BM–0.16 PT structure contains both large and tiny grains. The transverse size of the grain is mostly between 0.3 and 2.0 μm . Moreover, there are grains, which dimensions reach 7.0 μm . Grains' longitudinal dimensions vary from 0.2 μm to 12.0 μm (Figure 4a). In turn, the 0.76 BM–0.24 PT transverse size is mostly between 0.5 and 3.0 μm , while the grains' longitudinal size is between 1.0 and 5.5 μm (Figure 4b).

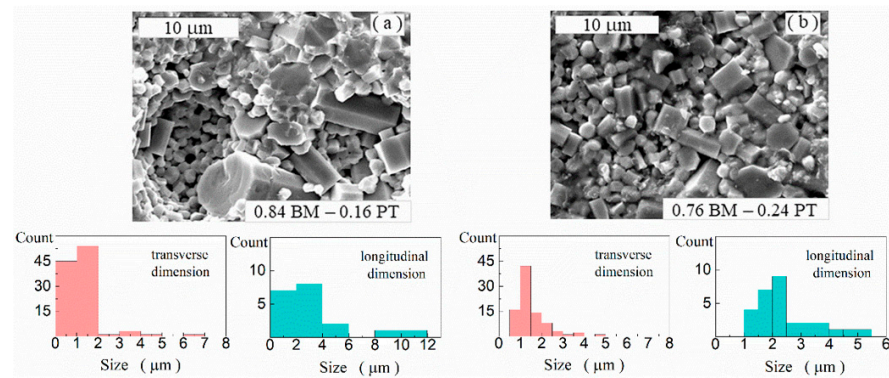


Figure 4. Secondary electron images obtained for 0.84 BM–0.16 PT ceramics (a) and 0.76 BM–0.24 PT ceramics (b). Histograms show grains' transverse and longitudinal size distribution.

The ceramic composites studied herein exhibit many caverns in the fracture surfaces (Figure 5). Such cavities are typical for the reference bismuth manganate ceramics [49]. Their origin would be associated with the technological process and attributed to chemical reactions. The occurrence of these cavities, where well-formed grains are visible, is one common feature of the BM-PT ceramics. The other common feature is porosity. We can distinguish well-shaped hexagon base polyhedrons grains, which are loosely attached to each other. Any clear tendency in size grain distribution in respect to PT content contribution was not observed for the BM-PT composite series. The majority of grains exhibited transverse size, which did not exceed 2.0 μm . The main number of grains showed longitudinal size lower than 7.0 μm . The exception occurred for 0.96 BM–0.04 PT and 0.84 BM–0.16 PT composition, where longitudinal size reached dimensions up to 12.0 μm . We attributed the occurrence of the small number of grains of sizes below 1.0 μm to the presence of the PT compound in the ceramics composite that is clearly visible for ceramics with higher content of PT.

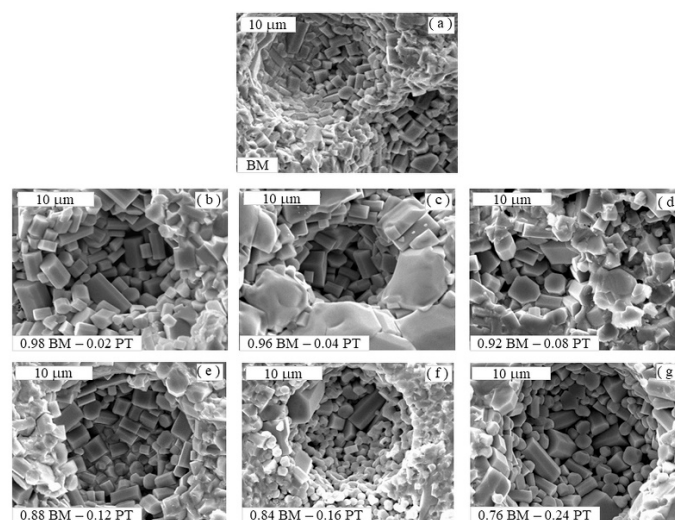


Figure 5. Secondary electron images obtained for the composite ceramics: BM (a), 0.98 BM–0.02 PT (b), 0.96 BM–0.04 PT (c), 0.92 BM–0.08 PT (d), 0.88 BM–0.12 PT (e), 0.84 BM–0.16 PT (f), and 0.76 BM–0.24 PT (g).

Survey spectra obtained for the reference BM and PT ceramics are shown in Figure 6. The BM sample showed the occurrence of manganate Mn, bismuth Bi, oxygen O, and gold Au. The occurrence of Au line relates to the gold-sputtered on the samples. The PT showed the occurrence of lead Pb, titanate Ti, O, and Au. The EDS analysis was performed for areas of $300 \times 300 \mu\text{m}^2$ (see Table 1). For the metal elements, the nominal chemical composition ratio is: Bi:Mn = 50.0:50.0 for BM ceramics, and Pb:Ti = 50.0:50.0 for perovskite PT. The EDS analysis showed, for BM ceramics, a real composition close to the nominal one. In the case of PT we observed a higher amount of Ti. This effect could be related to the evaporation of Pb during the sintering because of the high volatility of lead oxides. For BM-PT ceramics, survey spectra are shown in Figure 7. The samples showed the occurrence of Mn, Bi, Ti, Pb, and Au. The EDS analysis for Pb and Bi content is vague because of similar energy for these two elements. Hence, quantitative estimation suffers from overlapping of Pb and Bi most intensive lines in the analyzed spectrum. However, the obtained element content is close to expected. There are no impurities detected in all studies samples.

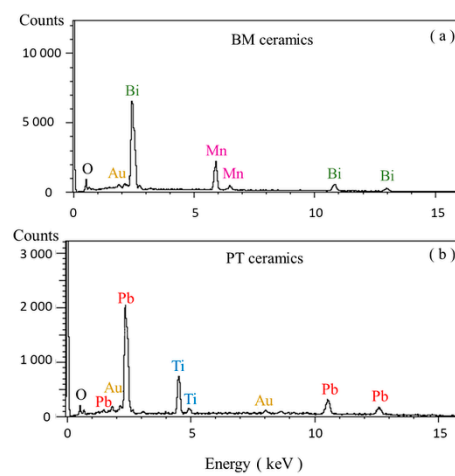


Figure 6. The survey spectra obtained for: (a) BM and (b) PT ceramics.

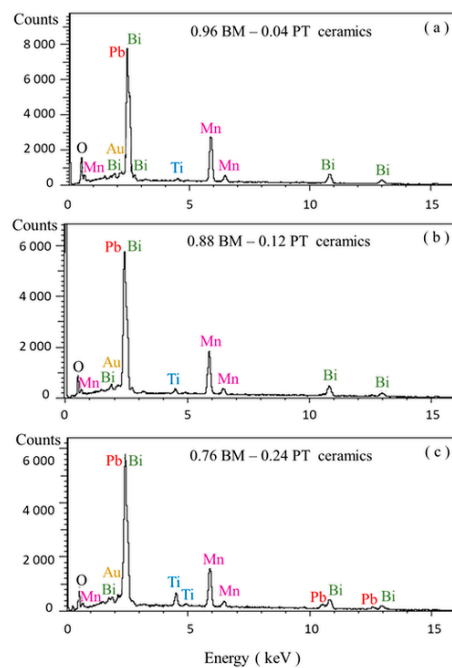


Figure 7. The survey spectra obtained for: (a) 0.96 BM–0.04 PT, (b) 0.88 BM–0.12 PT, and (c) 0.76 BM–0.24 PT ceramics.

Table 1. Exemplar atomic concentration (at%) estimated for chosen ceramics surfaces.

Atom	BM	Atom	PT	Atom	0.96 BM–0.04 PT	Atom	0.88 BM–0.12PT	Atom	0.76 BM–0.24 PT
Bi	50.2	Pb	48.5	Bi	45.0	Bi	43.6	Bi	36.5
Mn	49.8	Ti	51.5	Mn	51.4	Mn	45.1	Mn	38.3
				Pb	1.5	Pb	6.2	Pb	13.8
				Ti	2.1	Ti	5.1	Ti	11.4

3.2. Vis-NIR Optical Features

The room temperature diffuse reflectance R spectra were measured in the 400–1000 nm range of Vis-NIR spectrum. For the graphical estimation of the difference in energy states, E_{gap} , magnitude, the Vis-NIR spectra recorded in the R mode were transformed to Kubelka-Munk equation:

$$F(R) = (1 - R)^2 / 2R \quad (1)$$

which is proportional to the extinction coefficient, α . Determination of E_{gap} was conducted using the Tauc method and relation of incident photon energy, $E = h\nu$, with the modified Kubelka-Munk function:

$$(\alpha \cdot h\nu)^{1/n} \approx B(h\nu - E_{\text{gap}}) \quad (2)$$

We presumed the indirect allowed transitions in the BM-PT composite. Hence, $(\alpha \cdot h\nu)^{1/n}$ vs. $h\nu$ plots, where exponent $n = 2$, were applied for analysis. The E_{gap} was estimated by extrapolating the straight-line segment to the intersection with the $h\nu$ axis, that is for $(\alpha h\nu)^{1/2} = 0$ [51,52].

We note that the PT, BiMn_2O_5 , $\text{Bi}_{12}\text{MnO}_{20}$, and their derivative phases, which resulted from sintering, bring in individual electronic structure contributions. Moreover, the mutual migration ions and V_{O} defects may introduce intermediate band gap states and tails in the vicinity of the VB and conductivity band, CB, [24,43]. Therefore, any superposition spectrum, obtained for a doping-modified and two-phase semiconductor, is the 'effective' linear combination of the spectra of both components:

$$(\alpha(h\nu))_{\text{eff}} = a \cdot \alpha_1(h\nu) + b \cdot \alpha_2(h\nu) \quad (3)$$

where a and b determine the components' concentrations contributions, while $\alpha_1(h\nu)$ and $\alpha_2(h\nu)$ are the absorption coefficients of the assumed two phases contribution [6,44,52,53]. Therefore, an effective energy gap is determined using the Tauc relation:

$$\{[(\alpha(h\nu))_{\text{eff}}] h\nu\}^{1/2} = B(h\nu - E_{\text{gap}}) \quad (4)$$

Following the proposed approximation, we decided to conduct the spectra analysis using the Tauc method [44,51]. We performed extrapolation where straight-line slopes could be distinguished.

The diffuse reflectance spectra of BM and PT reference ceramics are shown in Figure 8. The $R(\lambda)$ increased when wavelength increased, more steeply for $\lambda > 900$ nm. A broad hump occurred in ~550–800 nm range, corresponding to red and dark red light. The most distinct difference occurred in the 400–550 nm range, where PT reflectance exhibited a steep change in R magnitude, contrary to the BM sample.

We discerned the straight-line segment in the Tauc plot obtained for the reference BM self-composite, and $E_{\text{gap}}(\text{NIR}) = 1.20$ eV was estimated for the NIR spectrum range (Figure 9a). $E_{\text{gap}}(\text{Vis}) = 2.45$ eV was estimated in the case of the reference PT compound (Figure 9b).

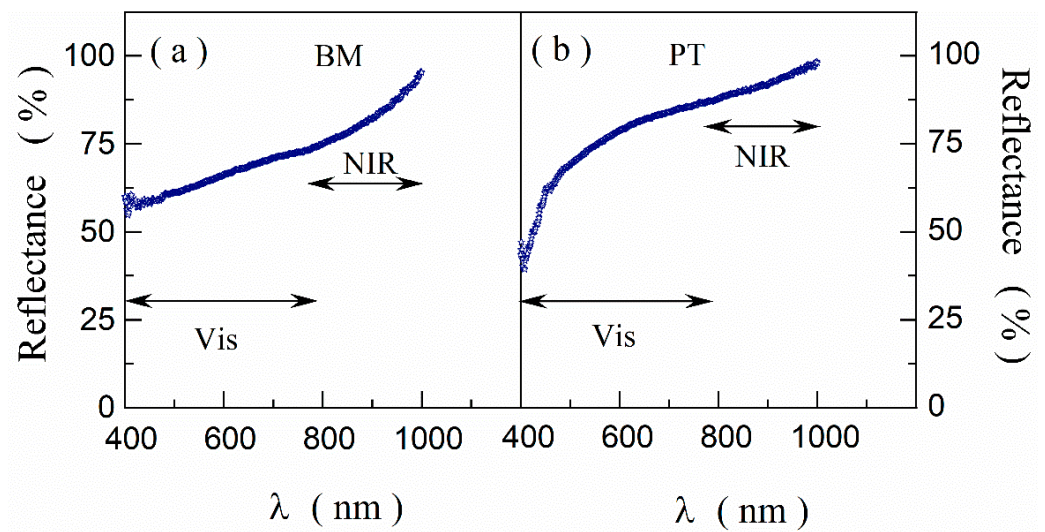


Figure 8. Reflectance, R , vs. wavelengths, λ , dependence measured for BM (a) and PT (b).

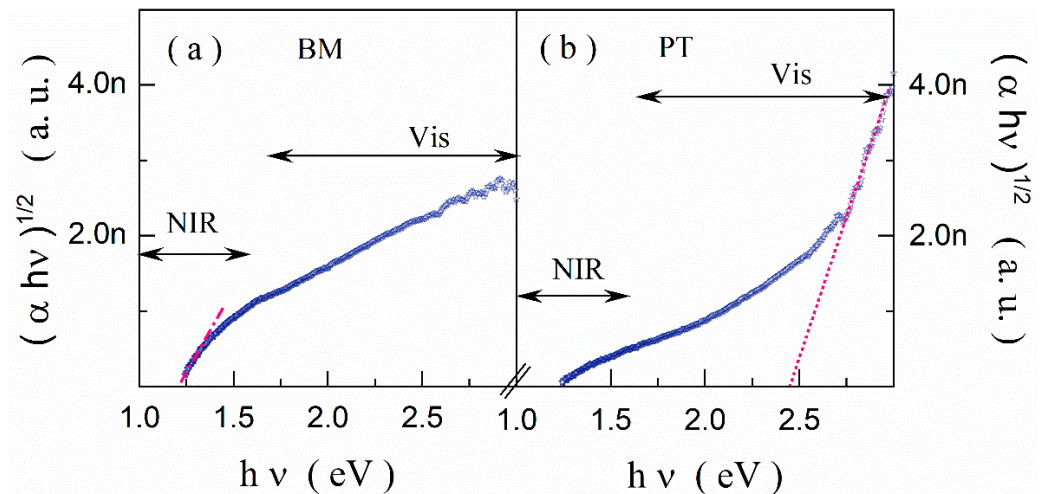


Figure 9. Modified Kubelka-Munk function $(\alpha hv)^{1/2}$ vs. photon energy $h\nu$ plot obtained for BM (a) and PT (b).

$R(\lambda)$ spectra obtained for $(1 - x)$ BM- x PT composites are shown in Figure 10. R magnitude decreased when the PT content increased, from ~50–80% to ~25–30% despite that the reference PT $R(\lambda)$ varied in the 40–100 % range (compare Figures 6 and 8). The $R(\lambda)$ common feature was its magnitude increase when wavelength increased and a more steep change in R magnitude for $\lambda > 900$ nm. A more or less distinct broad hump occurred in ~550–800 nm range; it shifted toward NIR range and became negligible for high content of PT component.

Graphical representation of the modified Kubelka–Munk function allowed us to determine E_{gap} magnitude dependence on the $(1 - x)$ BM- x PT ceramics composition (Figures 11 and 12). The $E_{\text{gap}}(\text{NIR})$ of the order of ~1 eV was estimated for BM-PT ceramics, and it showed a tendency to fluctuate with PT content change (Figure 12).

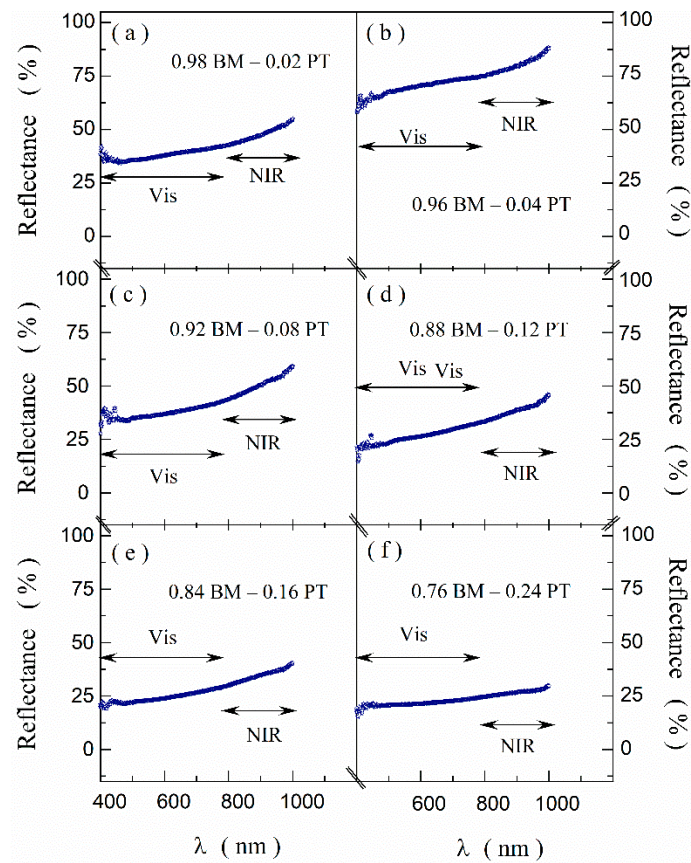


Figure 10. Reflectance, R , vs. wavelengths, λ , dependence measured for $(1 - x)$ BM- x PT ceramics, $x = 0.02, 0.04, 0.08, 0.12, 0.16, 0.24$, (a–f), respectively.

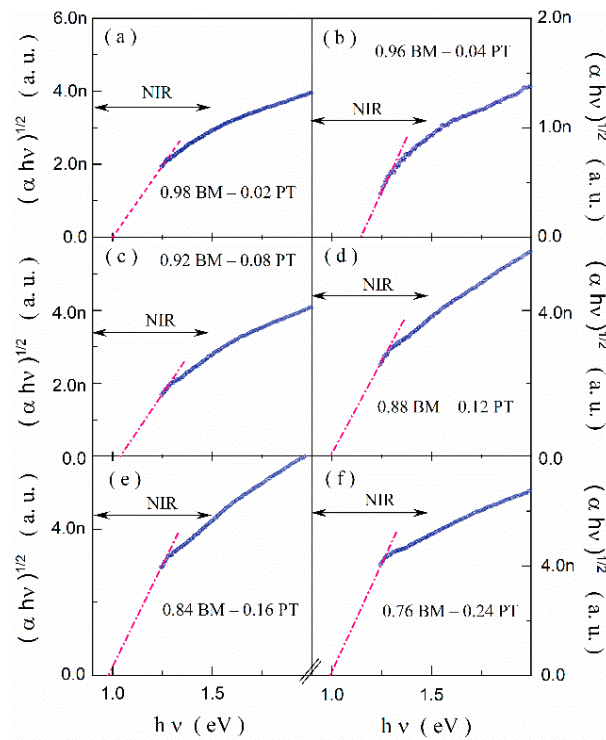


Figure 11. Modified Kubelka-Munk function $(\alpha hv)^{1/2}$ vs. photon energy $h\nu$ plot obtained for $(1 - x)$ BM- x PT ceramics, $x = 0.02, 0.04, 0.08, 0.12, 0.16, 0.24$, (a–f), respectively.

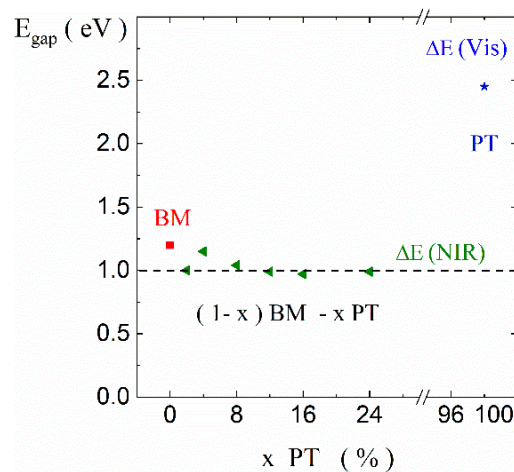


Figure 12. Optical energy gaps estimated for BM, PT, and $(1 - x)$ BM- x PT ceramic composites ($x = 0.02, 0.04, 0.08, 0.12, 0.16,$ and 0.24).

4. Discussion

The reference for PT ceramics was the one-phase compound. The light-yellow color of this material suggested that the actual E_{gap} magnitude originated from a defected PT structure would be lower from $E_{\text{gap}} = 3.4$ eV reported for the ideal stoichiometric transparent crystal [29,30]. We note that the $E_{\text{gap}} = 3.4$ eV of such PT can only be detected in the UV range, which was beyond our study frames. Hence, the $E_{\text{gap}}(\text{Vis}) = 2.45$ eV (Figure 9b) should correspond to the effects of defects and disorder. One notes that V_{O} defects introduce shallow and deep energy levels in the perovskite ABO_3 structures [24]. Such deduction also is justified by the literature reports. It is consistent with the results of calculations provided for defected PT, reported in the literature, where the full potential linearized augmented plane-wave calculation exhibited that oxygen vacancies induce additional in-gap Ti 3d states -1.1 eV below the Fermi energy [54]. Indirect optical gap varied from 2.78 eV to 3.66 eV dependably on the PT surface termination [31,55]. The experimentally determined $E_{\text{gap}} = 2.6$ eV seems to be also related to the defects subsystem of PT [56]. Therefore, $E_{\text{gap}}(\text{Vis}) = 2.45$ eV should be attributed to the gap between the defect-induced sub-band and CB, which position and possible tails were determined by crystal lattice disorder. These literature E_{gap} data are shown in Figure 13.

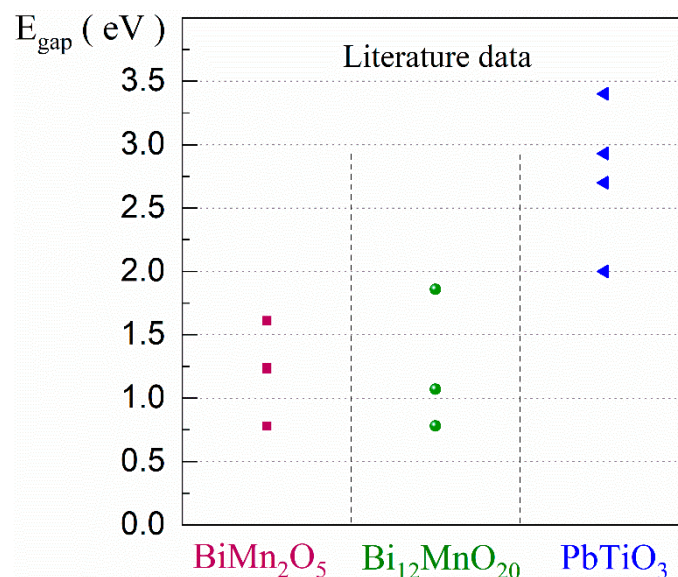


Figure 13. The diagram compares E_{gap} magnitudes, available from cited literature reports for BiMn_2O_5 , $\text{Bi}_{12}\text{MnO}_{20}$, and PbTiO_3 .

The BM and BM-PT ceramics are multi-phase composites [37,48,49]. BM is the self-composite consisting of the major BiMn_2O_5 and the minor $\text{Bi}_{12}\text{MnO}_{20}$ phase. The BM-PT composite consists of phases, which structure changed because of mutual migration of ions when the ceramics were sintered from the reference BM and PT [46,50]. For instance, it would be noted that the Bi_2O_3 phase, iso-structural with $\text{Bi}_{20}\text{TiO}_{32}$, transformed from the $\text{Bi}_{12}\text{MnO}_{20}$ parent phase of the BM self-composite [50]. Moreover, local fluctuations in composition and the occurrence of oxygen deficiency cannot be excluded. The graphite-black color of these BM-PT compounds indicated marked light absorbance in the Vis range.

Therefore, the measured $R(\lambda)$ spectra were considered as effective quantities, which included contributions from individual phases of the BM-PT system. It should be noted that the lower R magnitude occurred when the PT content in the BM-PT ceramics was higher. The R magnitude decrease from ~50–80% to ~25–30% indicated an active role of the PT component and influence porosity. Similar to a glassy black mirror, a standard flat and smooth surface usually offers reflectance on a 40–50% level. Lower R would be achieved in the case of a textured surface when light is scattered and absorbed more effectively [57]. It should be noticed that the SEM test exhibited porosity and concave voids in the BM-PT ceramics surfaces.

We note that the reference PT powder grain was much smaller than the BM-PT compounds grain (compare Figure 1b to Figures 1a, 2, 3, 4 and 5). Hence, we deduce that tiny grains of the PT powder introduced to the sintered BM-PT ceramics also would be responsible for this effect. We conclude that both the small grains of the PT component and the porous texture of BM-PT ceramics surface may facilitate scattering, decrease R to ~25%, and enhance light absorption. We noticed a correlation between R and ceramics morphology. The BM, 0.96 BM–0.04 PT, and PT ceramics showed R higher magnitude and more homogenous morphology than the other doped BM-PT ceramics. Moreover, the BM and PT samples were characterized by the smaller grains and the highest reflectance. Therefore, despite any uncontrolled and random factors that cannot be excluded *a priori*, we deduce that the low reflectance of the BM-PT ceramics can relate to the rough surface features.

We applied the Tauc procedure within the NIR following the assumed effective reflectance spectrum superposition obtained for the BM and BM-PT multi-phase composites [43,44,58]. The $E_{\text{gap}}(\text{NIR}) = 1.20$ eV, estimated for the BM self-composite, correlates to the literature data. The studied herein BM consists of the major BiMn_2O_5 phase and minor $\text{Bi}_{12}\text{MnO}_{20}$ phase. One notices that the $E_{\text{gap}} = 1.24$ eV was reported BiMn_2O_5 compound [44]. The case of $\text{Bi}_{12}\text{MnO}_{20}$ compound offers more possible charge transfers determined by Wu et al. [43]: the charge excitation between VB and CB of intrinsic $E_{\text{gap}} = 1.86$ eV, other from the VB to the intermediate band, IB, of ~0.79 eV, and also excitation from the intermediate band to the CB of ~1.07 eV (see Figure 13). Therefore, we do not assign the effective $E_{\text{gap}}(\text{NIR}) = 1.20$ eV to specific phase. Such the choice would be vague due to the similarity of the energy gap size; either $E_{\text{gap}} = 1.24$ eV of BiMn_2O_5 , or $E_{\text{gap}} = 1.07$ eV of $\text{Bi}_{12}\text{MnO}_{20}$ can be chosen. We note that the coincidence of estimated herein $E_{\text{gap}}(\text{NIR}) = 1.20$ eV to the literature reports on the perovskite BiMnO_3 compound ($E_{\text{gap}} = 1.1$ eV) is random due to this unstable perovskite phase was not detected in case of the studied herein BM. In the case of the $(1 - x)$ BM– x PT compounds, the obtained magnitude of E_{gap} fluctuated on $E_{\text{gap}}(\text{NIR}) = 1.00 \pm 0.15$ eV level (see Figure 12). We deduce an effective role of local disorder, which would influence the electronic structure of the studied material. The V_{O} occurrence would induce an additional sub-bands within the energy gap [24]. In case of the $\text{Bi}_{12}\text{MnO}_{20}$ phase, the V_{O} creates the IB band, mentioned above, which can be responsible for the charge transfer. However, in case of the BiMn_2O_5 , additional IB energy levels, leading to lower than 1 eV excitation energy, were not observed, using the applied NIR range. We propose that defects, most probably caused by mutual diffusion of ions between the phases, resulting from the final sintering procedure [46,50], create tails of states in the VB and CB that lead to the detected narrowing of the energy gap (see diagram in Figure 14).

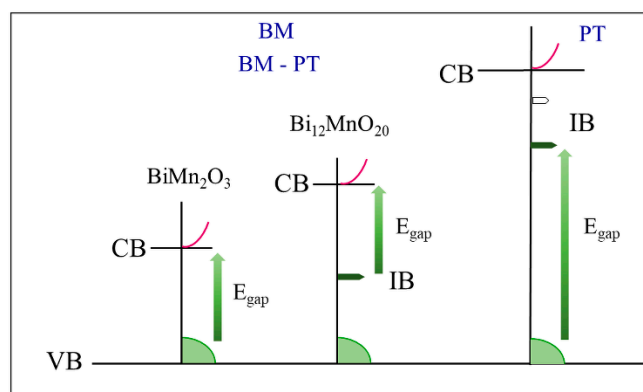


Figure 14. A schematic band, E_{gap} , layout proposed for BM, BM-PT, and PT ceramics, obtained from performed Vis-NIR test.

In summary, we would emphasize the most important properties of studied herein composite ceramics.

1. In the case of BM and PT reference materials, it was possible to attribute determined E_{gap} magnitudes to electric charge excitation from the VB to CB (BiMn_2O_5), to transition from IB to the CB ($\text{Bi}_{12}\text{MnO}_{20}$), and from VB to IB (PT);
2. The $(1 - x)$ BM- x PT composite exhibited $E_{\text{gap}}(\text{NIR}) = 1.00 \pm 0.15$ eV lower than E_{gap} magnitudes of the reference compounds. This gap narrowing effect originated from a disorder;
3. Determined properties of $(1 - x)$ BM- x PT, especially the narrowing of the E_{gap} magnitudes, of the order of 1 eV, which corresponds to marked light absorption in Vis and NIR, suggest potential optoelectrical applications.

Author Contributions: Conceptualization, A.M.; methodology, A.M., A.Z.S., J.K.; validation, A.M., A.Z.S., J.K.; formal analysis, A.M., A.Z.S.; investigation, A.M., A.Z.S., J.K.; writing—original draft preparation, A.M.; writing—review and editing, A.M., A.Z.S.; visualization, A.M., A.Z.S.; funding acquisition, A.M., A.Z.S. All authors have read and agreed to the published version of the manuscript.

Funding: A.M. and A.Z.S. note that this publication is co-financed by the funds granted under the Research Excellence Initiative of the University of Silesia in Katowice.

Institutional Review Board Statement: Not applicable.

Data Availability Statement: Not applicable.

Conflicts of Interest: The authors declare no conflict of interest.

References

1. Li, S.; Morasch, J.; Klein, A.; Chirila, C.; Pintilie, L.; Jia, L.; Ellmer, K.; Naderer, M.; Reichmann, K.; Gröting, M.; et al. Influence of orbital contributions to the valence band alignment of Bi_2O_3 , Fe_2O_3 , BiFeO_3 , and $\text{Bi}_{0.5}\text{Na}_{0.5}\text{TiO}_3$. *Phys. Rev. B* **2013**, *88*, 045428. [[CrossRef](#)]
2. Rühle, S. Tabulated values of the Shockley—Queisser limit for single junction solar cells. *Sol. Energy* **2016**, *130*, 139–147. [[CrossRef](#)]
3. Ehrler, B.; Alarcón-Lladó, E.; Tabernig, S.W.; Veeken, T.; Garnett, E.C.; Polman, A. Photovoltaics Reaching for the Shockley—Queisser Limit. *ACS Energy Lett.* **2020**, *5*, 3029–3033. [[CrossRef](#)]
4. Genenko, Y.A.; Glaum, J.; Hoffmann, M.J.; Albe, K. Mechanisms of aging and fatigue in ferroelectrics. *Mater. Sci. Eng. B* **2015**, *192*, 52–82. [[CrossRef](#)]
5. Grinberg, I.; West, D.V.; Torres, M.; Gou, G.; Stein, D.M.; Wu, L.; Chen, G.; Gallo, E.M.; Akbashev, A.R.; Davies, P.K.; et al. Perovskite oxides for visible-light-absorbing ferroelectric and photovoltaic materials. *Nature* **2013**, *503*, 509–512. [[CrossRef](#)]
6. Sheikh, M.S.; Ghosh, D.; Bhowmik, T.K.; Dutta, A.; Bhattacharyya, S.; Sinha, T.P. When multiferroics become photoelectrochemical catalysts: A case study with $\text{BiFeO}_3/\text{La}_2\text{NiMnO}_6$. *Mater. Chem. Phys.* **2020**, *244*, 122685. [[CrossRef](#)]
7. Li, P.; Abe, H.; Ye, J. Band-Gap Engineering of NaNbO_3 for Photocatalytic H_2 Evolution with Visible Light. *Int. J. Photoenergy* **2014**, *2014*, 380421. [[CrossRef](#)]
8. Hwang, D.W.; Kim, H.G.; Lee, J.S.; Kim, J.; Li, W.; Oh, S.H. Photocatalytic Hydrogen Production from Water over M-Doped $\text{La}_2\text{Ti}_2\text{O}_7$ ($M = \text{Cr, Fe}$) under Visible Light Irradiation ($\lambda > 420$ nm). *J. Phys. Chem. B* **2005**, *109*, 2093–2102. [[CrossRef](#)]

9. Ma, C.; Liu, Z.; Cai, Q.; Han, C.; Tong, Z. ZnO photoelectrode simultaneously modified with Cu₂O and Co-Pi based on broader light absorption and efficiently photogenerated carrier separation. *Inorg. Chem. Front.* **2018**, *5*, 2571–2578. [[CrossRef](#)]
10. Madusanka, H.T.D.S.; Herath, H.M.A.M.; Fernando, C.A.N. High photoresponse performance of self-powered n-Cu₂O/p-CuI heterojunction based UV-Visible photodetector. *Sens. Actuators A Phys.* **2019**, *296*, 61–69. [[CrossRef](#)]
11. He, L.; Fei, M.; Chen, J.; Tian, Y.; Jiang, Y.; Huang, Y.; Xu, K.; Hu, J.; Zhao, Z.; Zhang, Q.; et al. Graphitic C₃N₄ quantum dots for next-generation QLED displays. *Mater. Today* **2019**, *22*, 76–84. [[CrossRef](#)]
12. Wang, D.; Ye, J.; Kako, T.; Kimura, T. Photophysical and Photocatalytic Properties of SrTiO₃ Doped with Cr Cations on Different Sites. *J. Phys. Chem. B* **2006**, *110*, 15824–15830. [[CrossRef](#)] [[PubMed](#)]
13. Bujakiewicz-Koronska, R.; Nalecz, D.M.; Molak, A.; Budziak, A. DOS calculation for stoichiometric and oxygen defected (Bi_{1/2}Na_{1/2})(Mn_{1/2}Nb_{1/2})O₃. *Ferroelectrics* **2014**, *463*, 48–56. [[CrossRef](#)]
14. Shi, H.; Li, X.; Iwai, H.; Zou, Z.; Ye, J. 2-Propanol photodegradation over nitrogen-doped NaNbO₃ powders under visible-light irradiation. *J. Phys. Chem. Solids* **2009**, *70*, 931–935. [[CrossRef](#)]
15. Zheng, D.; Deng, H.; Pan, Y.; Guo, Y.; Zhao, F.; Yang, P.; Chu, J. Modified multiferroic properties in narrow bandgap (1 – x)BaTiO₃-xBaNb_{1/3}Cr_{2/3}O_{3-δ} ceramics. *Ceram. Int.* **2020**, *46*, 26823–26828. [[CrossRef](#)]
16. Varignon, J.; Bibes, M.; Zunger, A. Origin of band gaps in 3d perovskite oxides. *Nat. Commun.* **2019**, *10*, 1658. [[CrossRef](#)]
17. Chen, L.; Zheng, G.; Yao, G.; Zhang, P.; Dai, S.; Jiang, Y.; Li, H.; Yu, B.; Ni, H.; Wei, S. Lead-Free Perovskite Narrow-Bandgap Oxide Semiconductors of Rare-Earth Manganates. *ACS Omega* **2020**, *5*, 8766–8776. [[CrossRef](#)]
18. Butson, J.D.; Narangari, P.R.; Lysevych, M.; Wong-Leung, J.; Wan, Y.; Karuturi, S.K.; Tan, H.H.; Jagadish, C. InGaAsP as a Promising Narrow Band Gap Semiconductor for Photoelectrochemical Water Splitting. *ACS Appl. Mater. Interfaces* **2019**, *11*, 25236–25242. [[CrossRef](#)]
19. Sathe, A.; Seki, M.; Zhou, H.; Chen, J.X.; Tabata, H. Bandgap engineering in V-substituted α-Fe₂O₃ photoelectrodes. *Appl. Phys. Express* **2019**, *12*, 091003. [[CrossRef](#)]
20. Gadhomi, F.; Kallel, I.; Benzarti, Z.; Abdelmoula, N.; Hamedoun, M.; Elmoussaoui, H.; Mezzane, D.; Khemakhem, H. Investigation of magnetic, dielectric and optical properties of BiFe_{0.5}Mn_{0.5}O₃ multiferroic ceramic. *Chem. Phys. Lett.* **2020**, *753*, 137569. [[CrossRef](#)]
21. Molak, A.; Pilch, M. Visible light absorbance enhanced by nitrogen embedded in the surface layer of Mn-doped sodium niobate crystals, detected by ultra violet—visible spectroscopy, x-Ray photoelectron spectroscopy, and electric conductivity tests. *J. Appl. Phys.* **2016**, *119*, 204901. [[CrossRef](#)]
22. Mefford, J.T.; Hardin, W.G.; Dai, S.; Johnston, K.P.; Stevenson, K.J. Anion charge storage through oxygen intercalation in LaMnO₃ perovskite pseudocapacitor electrodes. *Nat. Mater.* **2014**, *13*, 726–732. [[CrossRef](#)] [[PubMed](#)]
23. Huang, Y.; Wei, Y.; Cheng, S.; Fan, L.; Li, Y.; Lin, J.; Wu, J. Photocatalytic property of nitrogen-doped layered perovskite K₂La₂Ti₃O₁₀. *Sol. Energy Mater. Sol. Cells* **2010**, *94*, 761–766. [[CrossRef](#)]
24. Prosandeyev, S.A.; Teslenko, N.M.; Fisenko, A. V Breaking of symmetry of one-electron orbitals at oxygen vacancies in perovskite-type oxides. *J. Phys. Condens. Matter* **1993**, *5*, 9327–9344. [[CrossRef](#)]
25. Srivastava, S. Study of Band Gap Tunability in one-dimensional Photonic Crystals of Multiferroic-dielectric materials: Case Study in Near Infrared Region. *SOP Trans. Appl. Phys.* **2014**, *2014*, 22–32. [[CrossRef](#)]
26. Benjwal, P.; Kar, K.K. Removal of methylene blue from wastewater under a low power irradiation source by Zn, Mn co-doped TiO₂ photocatalysts. *RSC Adv.* **2015**, *5*, 98166–98176. [[CrossRef](#)]
27. Xu, X.S.; Ihlefeld, J.F.; Lee, J.H.; Ezekoye, O.K.; Vlahos, E.; Ramesh, R.; Gopalan, V.; Pan, X.Q.; Schlom, D.G.; Musfeldt, J.L. Tunable band gap in Bi(Fe_{1-x}Mn_x)O₃ films. *Appl. Phys. Lett.* **2010**, *96*, 192901. [[CrossRef](#)]
28. Mocherla, P.S.V.; Karthik, C.; Ubig, R.; Ramachandra Rao, M.S.; Sudakar, C. Tunable bandgap in BiFeO₃ nanoparticles: The role of microstrain and oxygen defects. *Appl. Phys. Lett.* **2013**, *103*, 022910. [[CrossRef](#)]
29. Niu, P.J.; Yan, J.L.; Xu, C.Y. First-principles study of nitrogen doping and oxygen vacancy in cubic PbTiO₃. *Comput. Mater. Sci.* **2015**, *98*, 10–14. [[CrossRef](#)]
30. Zametin, V.I. Absorption Edge Anomalies in Polar Semiconductors and Dielectrics at Phase Transitions. *Phys. Status Solidi* **1984**, *124*, 625–640. [[CrossRef](#)]
31. Piskunov, S.; Kotomin, E.A.; Heifets, E.; Maier, J.; Eglitis, R.I.; Borstel, G. Hybrid DFT calculations of the atomic and electronic structure for ABO₃ perovskite (001) surfaces. *Surf. Sci.* **2005**, *575*, 75–88. [[CrossRef](#)]
32. Molak, A.; Wójcik, K. Optic properties and EPR spectra of PbTiO₃:Mn crystals. *Ferroelectrics* **1992**, *125*, 349–354. [[CrossRef](#)]
33. Leonarska, A.; Ujma, Z.; Molak, A. Nano-size grain powders and ceramics of PbTiO₃ obtained by the hydrothermal method and their electrical properties. *Ferroelectrics* **2014**, *466*, 42–50. [[CrossRef](#)]
34. Belik, A.A. Polar and nonpolar phases of BiMO₃: A review. *J. Solid State Chem.* **2012**, *195*, 32–40. [[CrossRef](#)]
35. Samuel, V.; Navale, S.C.; Jadhav, A.D.; Gaikwad, A.B.; Ravi, V. Synthesis of ultrafine BiMnO₃ particles at 100 °C. *Mater. Lett.* **2007**, *61*, 1050–1051. [[CrossRef](#)]
36. Molak, A.; Mahato, D.K.; Szeremeta, A.Z. Synthesis and characterization of electrical features of bismuth manganite and bismuth ferrite: Effects of doping in cationic and anionic sublattice: Materials for applications. *Prog. Cryst. Growth Charact. Mater.* **2018**, *64*, 1–22. [[CrossRef](#)]
37. Pilch, M.; Molak, A.; Koperski, J.; Zajdel, P. Influence of nitrogen flow during sintering of bismuth manganite ceramics on grain morphology and surface disorder. *Phase Transit.* **2017**, *90*, 112–124. [[CrossRef](#)]

38. Muñoz, A.; Alonso, J.A.; Casais, M.T.; Martínez-Lope, M.J.; Martínez, J.L.; Fernández-Díaz, M.T. Magnetic structure and properties of BiMn₂O₅. *Phys. Rev. B* **2002**, *65*, 144423. [[CrossRef](#)]
39. Chakrabartty, J. Oxide Perovskites for Solar Energy Conversion. Ph.D. Thesis, University of Quebec, Quebec, QC, Canada, 2018.
40. Gaikwad, V.M.; Goyal, S.; Yanda, P.; Sundaresan, A.; Chakraverty, S.; Ganguli, A.K. Influence of Fe substitution on structural and magnetic features of BiMn₂O₅ nanostructures. *J. Magn. Magn. Mater.* **2018**, *452*, 120–128. [[CrossRef](#)]
41. Zhang, J.; Xu, B.; Li, X.F.; Yao, K.L.; Liu, Z.L. Origin of the multiferroicity in BiMn₂O₅ from first-principles calculations. *J. Magn. Magn. Mater.* **2011**, *323*, 1599–1605. [[CrossRef](#)]
42. Li, N.; Yao, K.; Gao, G.; Sun, Z.; Li, L. Charge, orbital and spin ordering in multiferroic BiMn₂O₅: Density functional theory calculations. *Phys. Chem. Chem. Phys.* **2011**, *13*, 9418. [[CrossRef](#)] [[PubMed](#)]
43. Wu, X.; Li, M.; Li, J.; Zhang, G.; Yin, S. A sillenite-type Bi₁₂MnO₂₀ photocatalyst: UV, visible and infrared lights responsive photocatalytic properties induced by the hybridization of Mn 3d and O 2p orbitals. *Appl. Catal. B Environ.* **2017**, *219*, 132–141. [[CrossRef](#)]
44. Chakrabartty, J.P.; Nechache, R.; Harnagea, C.; Rosei, F. Photovoltaic effect in multiphase Bi-Mn-O thin films. *Opt. Express* **2014**, *22*, A80. [[CrossRef](#)] [[PubMed](#)]
45. Szeremeta, A.Z.; Pawlus, S.; Nowok, A.; Grzybowska, K.; Zubko, M.; Molak, A. Hydrostatic pressure influence on electric relaxation response of bismuth manganite ceramics. *J. Am. Ceram. Soc.* **2020**, *103*, 3732–3738. [[CrossRef](#)]
46. Szeremeta, A.Z.; Nowok, A.; Zubko, M.; Pawlus, S.; Gruszka, I.; Koperski, J.; Molak, A. Influence of interfacial stresses on electrical properties of bismuth manganite—lead titanate—epoxy composite. *Ceram. Int.* **2021**, *47*, 34619–34632. [[CrossRef](#)]
47. Szeremeta, A.Z. Relaxation Processes in Bismuth Manganite Which Was a Matrix for PbTiO₃ or Was Doped to Pb(Zr_{0.70}Ti_{0.30})O₃ Ceramics. Ph.D. Thesis, University of Silesia, Katowice, Poland, 2018. (In Polish).
48. Molak, A.; Leonarska, A.; Szeremeta, A. Electric current relaxation and resistance switching in non-homogeneous bismuth manganite. *Ferroelectrics* **2015**, *485*, 161–172. [[CrossRef](#)]
49. Molak, A.; Ujma, Z.; Pilch, M.; Gruszka, I.; Pawelczyk, M. Resistance switching induced in BiMnO₃ ceramics. *Ferroelectrics* **2014**, *464*, 59–71. [[CrossRef](#)]
50. Molak, A.; Szeremeta, A.Z.; Zubko, M.; Nowok, A.; Balin, K.; Gruszka, I.; Pawlus, S. Influence of hydrostatic pressure on electrical relaxation in non-homogeneous bismuth manganite—Lead titanate ceramics. *J. Alloys Compd.* **2021**, *854*, 157219. [[CrossRef](#)]
51. López, R.; Gómez, R. Band-gap energy estimation from diffuse reflectance measurements on sol–gel and commercial TiO₂: A comparative study. *J. Sol-Gel Sci. Technol.* **2012**, *61*, 1–7. [[CrossRef](#)]
52. Zanatta, A.R. Revisiting the optical bandgap of semiconductors and the proposal of a unified methodology to its determination. *Sci. Rep.* **2019**, *9*, 11225. [[CrossRef](#)]
53. Makuła, P.; Pacia, M.; Macyk, W. How to Correctly Determine the Band Gap Energy of Modified Semiconductor Photocatalysts Based on UV–Vis Spectra. *J. Phys. Chem. Lett.* **2018**, *9*, 6814–6817. [[CrossRef](#)]
54. Cai, M.-Q.; Tang, C.-H.; Tan, X.; Deng, H.-Q.; Hu, W.-Y.; Wang, L.-L.; Wang, Y.-G. First-principles study for the atomic structures and electronic properties of PbTiO₃ oxygen-vacancies (001) surface. *Surf. Sci.* **2007**, *601*, 5412–5418. [[CrossRef](#)]
55. de Lazaro, S.; Longo, E.; Sambrano, J.R.; Beltrán, A. Structural and electronic properties of PbTiO₃ slabs: A DFT periodic study. *Surf. Sci.* **2004**, *552*, 149–159. [[CrossRef](#)]
56. Gerges, M.K.; Mostafa, M.; Rashwan, G.M. Structural, optical and electrical properties of PbTiO₃ nanoparticles prepared by Sol-Gel method. *Int. J. Latest Res. Eng. Technol.* **2016**, *2*, 42–49.
57. Zhong, J.; Wu, W.; Liao, J.; Feng, W.; Jiang, Y.; Wang, L.; Kuang, D. The Rise of Textured Perovskite Morphology: Revolutionizing the Pathway toward High-Performance Optoelectronic Devices. *Adv. Energy Mater.* **2020**, *10*, 1902256. [[CrossRef](#)]
58. Shamitha, C.; Senthil, T.; Wu, L.; Kumar, B.S.; Anandhan, S. Sol–gel electrospun mesoporous ZnMn₂O₄ nanofibers with superior specific surface area. *J. Mater. Sci. Mater. Electron.* **2017**, *28*, 15846–15860. [[CrossRef](#)]